ACS APPLIED MATERIALS & INTERFACES

Research Article

www.acsami.org

Nanoscale Characterization of TiO_2 Films Grown by Atomic Layer Deposition on RuO_2 Electrodes

Katsuhisa Murakami,[†,▽] Mathias Rommel,*[,‡] Boris Hudec,[§] Alica Rosová,[§] Kristína Hušeková,[§] Edmund Dobročka,[§] Raul Rammula,[∥] Aarne Kasikov,[∥] Jeong Hwan Han,[⊥,○] Woongkyu Lee,[⊥] Seul Ji Song,[⊥] Albena Paskaleva,[#] Anton J. Bauer,[‡] Lothar Frey,[†,‡] Karol Fröhlich,[§] Jaan Aarik,[∥] and Cheol Seong Hwang[⊥]

[†]Chair of Electron Devices, University of Erlangen-Nuremberg, Cauerstrasse 6, 91058 Erlangen, Germany

[‡]Fraunhofer Institute for Integrated Systems and Device Technology, Schottkystrasse 10, 91058 Erlangen, Germany

[§]Institute of Electrical Engineering, Slovak Academy of Sciences, Dúbravská Cesta 9, 84104 Bratislava, Slovakia

[∥]Institute of Physics, University of Tartu, Riia 142, 51014 Tartu, Estonia

[⊥]Department of Materials Science and Engineering, and Inter-university Semiconductor Research Center, Seoul National University, Seoul 151-744, Republic of Korea

[#]Institute of Solid State Physics, Bulgarian Academy of Sciences, 72 Tzarigradsko Chaussee, 1784 Sofia, Bulgaria

Supporting Information

ABSTRACT: Topography and leakage current maps of TiO_2 films grown by atomic layer deposition on RuO_2 electrodes using either a $TiCl_4$ or a $Ti(O\text{-}i\text{-}C_3H_7)_4$ precursor were characterized at nanoscale by conductive atomic force microscopy (CAFM). For both films, the leakage current flows mainly through elevated grains and not along grain boundaries. The overall CAFM leakage current is larger and more localized for the $TiCl_4$-based films (0.63 nm capacitance equivalent oxide thickness, CET) compared to the $Ti(O\text{-}i\text{-}C_3H_7)_4$-based films (0.68 nm CET). Both films have a physical thickness of ~20 nm. The nanoscale leakage currents are consistent with macroscopic leakage currents from capacitor structures and are correlated with grain characteristics observed by topography maps and transmission electron microscopy as well as with X-ray diffraction.

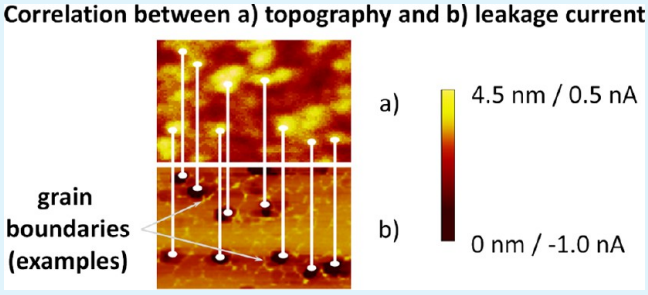

KEYWORDS: *high-k dielectrics, conductive AFM (CAFM), metal−insulator−metal (MIM) capacitor, TiO_2, RuO_2*

INTRODUCTION

Metal−insulator−metal (MIM) capacitors with TiO_2 dielectric films in rutile crystallographic form have been identified as a promising solution for capacitor in future dynamic random access memories (DRAM).[1,2] Rutile type TiO_2 films exhibit rather high dielectric constants above 100.[1] The rutile phase of TiO_2 is usually formed at a high-temperature regime (above 700 °C) if there are no other factors (e.g., epitaxial match to substrate) supporting the rutile phase formation. However, low-temperature growth techniques (below 500 °C) are required to adapt the rutile type TiO_2 films for DRAM applications according to the International Technology Roadmap for Semiconductors.[3] Due to the extreme three-dimensional geometry of the capacitors in DRAM, a film growth technique which can offer an excellent step coverage and atomic scale controllability is required for this application. Such requirements can be met by atomic layer deposition (ALD) processes, which usually require a low process temperature due to the limited thermal stability of some Ti-precursors.[4,5] In addition, TiO_2 is not a perfect insulator due to its relatively small band gap (approximately 3 eV) and excess conductivity caused by oxygen nonstochiometry.[6] Therefore, TiO_2 films suffer from enhanced leakage currents, in particular for thin films with a thickness of approximately 10 nm and below. Previously, it was shown that the rutile type TiO_2 films can be grown by ALD on oxidized Ru bottom electrodes at a low growth temperature (below 500 °C).[7,8] We also demonstrated that a post deposition annealing (PDA) in O_2 atmosphere was effective for a reduction of the leakage current of TiO_2 films.[9] Further adopting the RuO_2 bottom electrode grown by metal−organic chemical vapor deposition (MOCVD) technique resulted in an additional improvement of the leakage current characteristics.[2]

In our previous study,[10] we have compared $Pt/TiO_2/RuO_2$ MIM structures with rutile type TiO_2 dielectrics grown by two different ALD processes in terms of conventional macroscopic capacitance−voltage and current−voltage measurements. It was

Received: November 4, 2013
Accepted: January 31, 2014
Published: January 31, 2014

found that TiO_2 films grown using a $TiCl_4$-based process exhibited higher dielectric constant values but also higher leakage currents than films grown by a Ti-tetra-isopropoxide (TTIP or $Ti(O\text{-}i\text{-}C_3H_7)_4$)-based process. Recent development of the $TiCl_4$-based ALD process has allowed preparation of capacitor structures with undoped TiO_2 dielectrics that have shown leakage current densities markedly below 10^{-7} A/cm^2 at a bias of 0.8 V and capacitance equivalent oxide thicknesses (CET) of 0.45−0.50 nm.[11] These leakage current densities are well comparable to those measured for TiO_2 films, which had similar CET values but were deposited from TTIP and O_3 (see Figure 1). In the case of thicker films, the TTIP-O_3 process

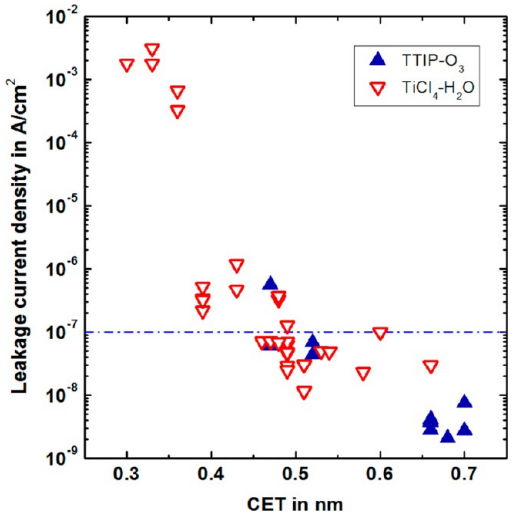

Figure 1. Leakage current density as a function of CET determined for TiO_2 thin films grown by ALD from TTIP and O_3 (ref 10) and from $TiCl_4$ and H_2O.[11] The dashed line corresponds to the maximum leakage current density at 0.6 V for DRAMs of the 20 nm node.[3]

allowed, however, obtaining leakage current densities significantly below 10^{-8} A/cm^2 while the corresponding parameter for films with comparable thicknesses deposited from $TiCl_4$ and H_2O stayed at levels exceeding 3×10^{-8} A/cm^2 (see Figure 1). The present study was performed in order to understand reasons for this difference and find approaches for further reduction of leakage currents in this kind of dielectrics.

Transmission electron microscopy (TEM) studies revealed that the microstructures of these two types of layers are different. The reason for the differences in the leakage current characteristics, however, could not fully be explained by TEM. In contrast to conventional SiO_2 dielectrics, leakage current distribution of high-k dielectrics is usually inhomogeneous due to the inhomogeneous crystallographic orientation of their grains, existing grain boundaries, and surface topography on the nanoscale. It is, therefore, important to investigate surface morphology and leakage currents of high-k dielectrics with a high lateral resolution simultaneously. In this work, we are comparing the nanoscale conductivity of different types of TiO_2 layers with 20 nm physical thickness by conductive atomic force microscopy (CAFM).

CAFM[12] is a powerful technique for the investigation of leakage currents through thin dielectric layers with nanoscale lateral resolution.[13−18] Applying a voltage between a conductive tip and the bottom electrode the current flowing through the dielectric is locally measured at nanoscale simultaneously with the surface topography. In this work, nanoscale leakage current distributions of TiO_2 films grown by two different ALD processes were measured by CAFM to investigate the origin of the difference in their leakage current characteristics.

EXPERIMENTAL SECTION

The TiO_2 films used in this work have been studied in a previous work in terms of macroscopic electrical measurements and TEM cross-section imaging.[10] The films were grown by ALD on 25 nm thick conducting RuO_2 bottom electrodes, which were prepared by metal organic chemical vapor deposition on Si(100) substrates with a 100 nm thick SiO_2 layer on top. One type of the TiO_2 films (sample name: $TiO_2(TiCl_4)$) was grown by ALD at 400 °C using $TiCl_4$ and H_2O as precursors.[1] The second type of TiO_2 films (sample name: TiO_2(TTIP)) was prepared by ALD at 250 °C using $Ti(O\text{-}i\text{-}C_3H_7)_4$ (TTIP) and ozone (concentration 250 g·m^{-3}) as Ti precursor and reactant gas, respectively.[2] Subsequently, for both samples, a PDA procedure was performed at 400 °C in a 5% O_2/N_2 gas mixture atmosphere. The physical thickness of both TiO_2 films was approximately 20 nm corresponding to a CET of 0.63 nm for the $TiO_2(TiCl_4)$ and 0.68 nm for the TiO_2(TTIP) sample, as obtained from conventional capacitance−voltage measurement analysis. The physical film thickness was confirmed by both TEM and X-ray reflectivity (XRR) measurements (see Figure S1 in the Supporting Information). For macroscopic electrical characterization, Pt top electrodes (area of approximately 5×10^4 μm^2) were prepared by electron beam evaporation through a shadow mask at room temperature. Macroscopic current−voltage characteristics were measured using a Keithley 2400 SourceMeter. The microstructures of the deposited films were studied by plane and cross-section view TEM on a JEOL JEM 1200 EX microscope with 120 kV accelerating voltage. Phase composition of the films was identified by X-ray diffraction (XRD) on Bruker AXS-D8 Discover diffractometer with a rotating anode at a grazing incidence angle of 1.5° using Cu Kα radiation. The XRR measurements were performed on the same equipment.

Topography and leakage current maps of TiO_2 films were simultaneously measured in ambient atmosphere by CAFM with a highly sensitive current amplifier (Dimension ICON with extended TUNA module, Bruker AXS) and Pt/Ir coated silicon tips (SD-EFM100, Nanosensors). The current amplifier has 4 current level sensitivities of 1 pA/V (approx. 40 fA to 12 pA), 10 pA/V (approx. 100 fA to 120 pA), 1 nA/V (approx. 100 pA to 12 nA), and 100 nA/V (approx. 500 pA to 1.2 μA). The current sensitivity can be changed by the operating software without the need to remove the tip from the sample. Therefore, leakage current maps can be obtained for a wide current range from approximately 40 fA to 1.2 μA at an identical scan area by applying various bias voltages and changing the current sensitivity appropriately. The nominal tip radius of the used Pt/Ir coated probes is less than 100 nm. For the CAFM measurements, the bottom electrode was negatively biased to avoid anodic oxidation of the sample surface in air. For each sample, a series of topography and leakage current maps at an identical scan area of 2×0.5 μm^2 was measured for applied biases ranging from −0.4 to −2.0 V with an increment of −0.1 V. It should be noted that using CAFM the contact resistance is higher than for conventional current−voltage measurements using relatively large metal electrodes. However, using CAFM for the characterization of dielectric thin films the overall current conduction is still largely affected by the film itself so that CAFM and conventional current density−voltage characteristics can be directly compared once the different work functions and the effective contact areas of the CAFM tip and the gate contact of the test structures for conventional measurements are accounted for.[15,19,20]

RESULTS AND DISCUSSION

Figure 2 shows plane view TEM images for sample $TiO_2(TiCl_4)$ (Figure 2a) and sample TiO_2(TTIP) (Figure 2b). The RuO_2 bottom electrodes of the samples were removed by ion milling during the TEM specimen preparation. The TEM images exclusively show the microstructure of the single

dx.doi.org/10.1021/am4049139 | ACS Appl. Mater. Interfaces 2014, 6, 2486−2492

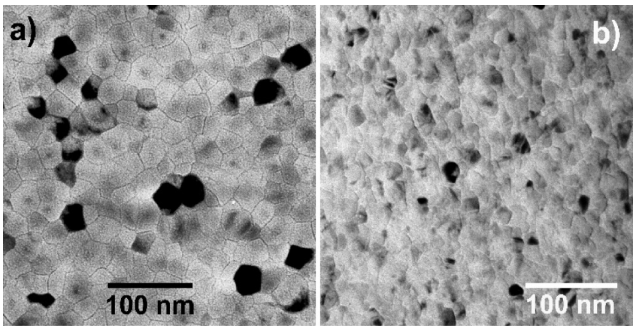

Figure 2. TEM image (plane view) of the TiO_2 films grown using (a) a $TiCl_4$ and (b) a TTIP precursor. Different brightness corresponds to different grain orientation.

rutile phase in the TiO_2 layers as confirmed by selected area electron diffraction (data not shown but the electron diffractions correspond to JCPDS 21-1276). It can be observed that sample $TiO_2(TiCl_4)$ is well crystallized. The corresponding TEM image exhibits a larger average TiO_2 grain size (mean diameter of 28 ± 6 nm), while the average TiO_2 grain size of sample TiO_2(TTIP) is smaller (mean diameter of 19 ± 5 nm). For the latter sample grain contrast is slightly blurred probably due to residual strain and/or increased presence of defects connected with incomplete phase crystallization, which can be understood from the lower ALD temperature (250 °C) compared to the $TiO_2(TiCl_4)$ sample (400 °C).

Figure 3 shows the correlation between topography and leakage current distribution for both TiO_2 films. In a first approximation, the topography maps of the films are comparable whereas the leakage current distributions differ significantly. The observed pronounced topography can be attributed to the roughness of the ruthenium oxide electrode as shown by TEM cross section images (see Figure 5).[10] From the CAFM maps in Figure 3, the major observations are: high leakage currents flow mainly through elevated TiO_2 grains (see also Figure S2 in the Supporting Information for superposition images of topography and high leakage current spots for higher applied voltages), and strongly reduced leakage currents can be observed at the TiO_2 grain boundaries which is important to note, as for other high-k films often increased currents are observed along grain boundaries.[13,21,22] As this is the case for both types of films, the difference in their leakage current densities from macroscopic characteristics[10] (see also Figure 4) cannot simply be attributed to a fundamentally different leakage current distribution (e.g., for one film type through grains[23,24] whereas for the other type along grain boundaries[13,21,22]). Finally, the average grain size for sample $TiO_2(TiCl_4)$ as observed from the topography and CAFM maps in Figure 3 is

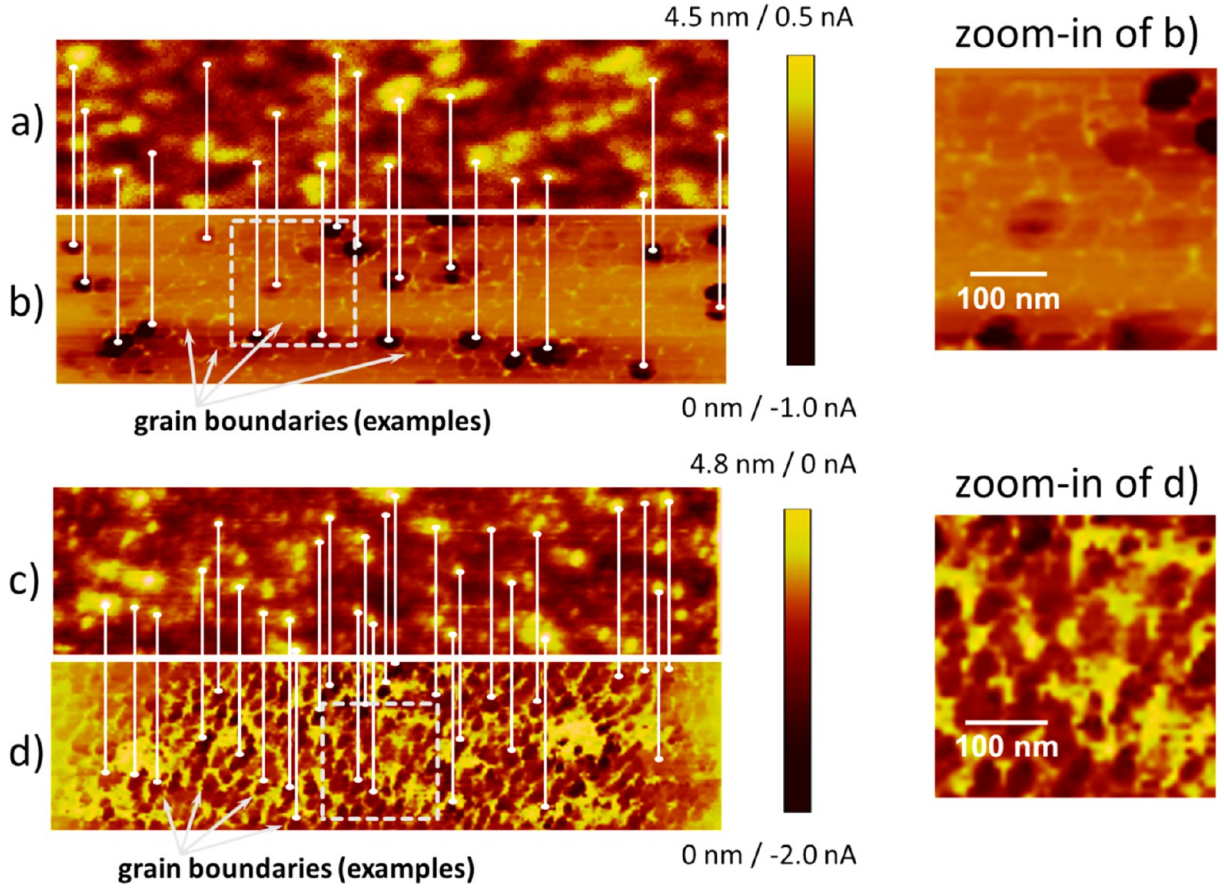

Figure 3. Correlation between topography and leakage current distribution. Topography maps of (a) sample $TiO_2(TiCl_4)$ and (c) sample TiO_2(TTIP). Leakage current distribution maps of (b) sample $TiO_2(TiCl_4)$ (applied bias voltage of −0.9 V, measured with 1 nA/V sensitivity) and (d) sample TiO_2(TTIP) (applied bias voltage of −1.8 V, measured with 1 nA/V sensitivity), acquired simultaneously with corresponding topography maps in (a) and (c). Scan area for maps (a−d) is 2 × 0.5 μm^2. On the right, zoom-in images of the leakage current maps (b) and (d) are presented (as indicated by the dashed frames in the original maps). Note that the current scale in (b) only includes positive currents to improve visibility. Actual currents do not exceed 0 A. The vertical lines point to corresponding areas in the topography and current maps.

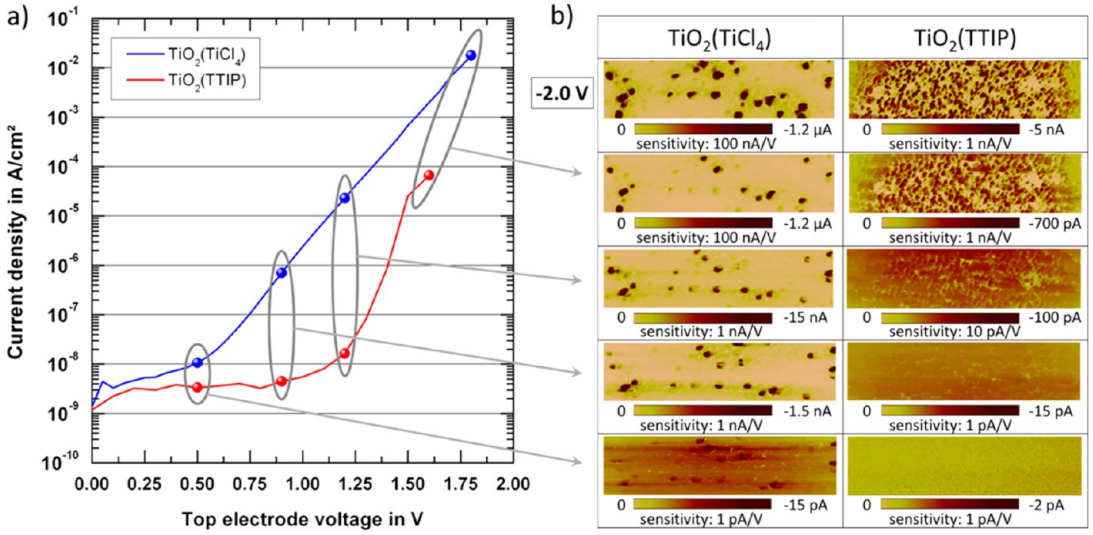

Figure 4. Comparison of macroscopic and nanoscale current characteristics. (a) Macroscopic current density voltage curves for TiO_2 MIM structures using a $TiCl_4$ and a TTIP precursor, respectively. The symbols indicate the points of the curves where CAFM maps with the same applied bias are shown in (b). (b) Leakage current distribution maps of samples $TiO_2(TiCl_4)$ and TiO_2(TTIP) with various applied bias voltages (in the top row, maps are shown for a bias voltage of −2.0 V applied to the bottom electrode). Note the different current scales. The scan area of all maps is 2 × 0.5 μm^2.

obviously larger than that for sample TiO_2(TTIP). It is important to note that the grain dimensions from the CAFM maps correlate well with the findings from plane view TEM analysis as shown in Figure 2 (see also the enlarged details of the leakage current maps in Figure 3 which have the same scale as the TEM plane view images in Figure 2) although the identification of grain boundaries is not that clear for the TTIP sample. Therefore, as the polycrystalline RuO_2 layer below the TiO_2 layers is identical for both samples, the CAFM maps reveal the characteristics of the TiO_2 layers and not the RuO_2 layer below which will later be discussed in some more detail. Probably, measurements in ultrahigh vacuum (UHV) with enhanced lateral resolution would have enabled a more direct identification of grains and grain boundaries.[20,25,26] The enhanced lateral resolution for UHV measurements is normally explained by the nonavoidable water meniscus between the tip and the sample in ambient which enlarges the effective contact area of the tip.[25]

Figure 4 shows a comparison of macroscopic and nanoscale current characteristics. From Figure 4a, the difference in the macroscopic current density−voltage characteristics of MIM capacitors for the differently deposited TiO_2 layers is clearly visible (the presented measurements are characteristics from single MIM capacitors which are representative for each sample). Sample TiO_2(TTIP) shows smaller leakage current densities than sample $TiO_2(TiCl_4)$ does. A series of current distribution maps of both samples for different applied bias voltages is shown in Figure 4b (see Figures S3 and S4 in the Supporting Information for a detailed series of topography and current distribution maps for both samples for biases ranging from −0.4 to −2.0 V with an increment of −0.1 V). Like in the case of particular voltages illustrated in Figure 3, all current distribution maps in Figure 4b correlate with topography reflecting the sample microstructure. Therefore, it can be confirmed that the leakage current distribution of the TiO_2 film deposited from a $TiCl_4$ precursor shows few localized relatively large grains with rather high leakage currents, while that deposited from a TTIP precursor shows a more homogeneous distribution of smaller grains with lower leakage currents. The CAFM leakage current distribution maps also reveal that the overall leakage currents for sample $TiO_2(TiCl_4)$ are significantly larger than those for sample TiO_2(TTIP) with the leakage currents through the leaky grains of the former sample being larger by up to more than 3 orders of magnitude compared to the latter sample (see Figure 4b). Thus, the nanoscale leakage current characteristics showed very good qualitative correlation with the macroscopic leakage current characteristics. In this context it should be noted that for CAFM applied voltages of 1 V and above are not critical as such for the investigated films and the overall voltage range applied by CAFM is very similar to that used for obtaining the current voltage characteristics of large area electrodes (see Figure 4a).

From the presented results, two important observations were found: First, the leakage current in both types of TiO_2 layers flows through grains, not along grain boundaries. The second observation is that the samples exhibit a different distribution of leakage current spots which show significantly different magnitudes of leakage current.

The first observation is connected with the morphology of both investigated layers. The root-mean-squared (RMS) roughness of the MOCVD grown 25 nm thick RuO_2 bottom electrode layers employed in this study was measured by AFM to be 1.94 nm. On the other hand, the RMS roughness values of TiO_2 layers deposited on top of RuO_2 were found to be 1.72 and 1.82 nm for the $TiCl_4$ and TTIP cases, respectively. RuO_2 layers tend to have an increased roughness due to faceting of RuO_2 grains on the surface. During local epitaxial growth of TiO_2 grains on RuO_2 grains,[1,10] the top surface of the resulting TiO_2 layers, however, becomes smoother. Thus, the thickness of the TiO_2 layer is larger above RuO_2 grain boundaries and smaller above RuO_2 grain tips as can be seen from Figure 5. Higher conduction through grains rather than grain boundaries can, thus, be partly explained for both samples by field enhancement effects due to lower dielectric thickness. Obviously, the grain size of the TiO_2 layers is not identical to that of the RuO_2 layer. Therefore, from a statistical point of

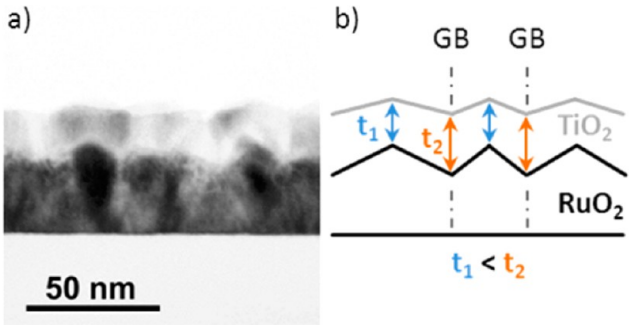

Figure 5. (a) TEM cross section image of sample $TiO_2(TiCl_4)$ on the polycrystalline RuO_2 layer grown by MOCVD. (b) Explanatory sketch: the TiO_2 is locally thicker over the RuO_2 grain boundaries and thinner over the RuO_2 grain tips with respect to the smoothening effect.

view there will be grain boundaries of the TiO_2 which are located on top of elevated RuO_2 grains (which define the location of the elevated spots of the overall sample) and, thus, not all elevated spots in topography coincide with high leakage current spots. These effects are statistically more relevant for the sample with smaller grains (i.e., the TTIP sample).

In this context, it should be pointed out that the CAFM maps should reflect a very similar grain structure if the TiO_2 film thickness would exclusively determine the leakage current. This grain structure would reflect the RuO_2 topography, which is identical for both samples (see Figure 5). As this is obviously not the case, the main differences in the observed leakage patterns are due to the different TiO_2 films and reveal the structure of the TiO_2 layers (i.e., observed grain boundaries in CAFM belong to TiO_2 GBs). However, the superposition of the effect of inhomogeneous TiO_2 film thickness has also to be accounted for.

Another reason for the increased leakage current through the grains compared to grain boundaries for both samples could be related to an inhomogeneous distribution of oxygen and oxygen vacancies (V_O). Concerning V_O in the grains, they affect the magnitude of the leakage current in several ways. V_O are double positively charged, which increases the internal field and, consequently, also the leakage current.[27] V_O serve as stepping sites for electrons, thus enhancing the trap-assisted tunneling (TAT) and giving rise to a higher leakage current. Although the origin and the exact conduction mechanisms for leakage currents in TiO_2 thin films are still not fully understood, TAT was recently proposed as a dominant mechanism.[28] Finally, oxygen vacancies are known to form dipoles which act to reduce the effective work function (EWF) of the metal electrode resulting in increased leakage currents. When the concentration of V_O is very high they were predicted to agglomerate in Magnéli phases.[29] The actual presence of these phases in our films, however, is unlikely since they are usually formed under an extremely reducing atmosphere, for high growth rates with diffusion limiting growth mode[30] or under high electric field.[31] In addition, no evidence for the presence of such phases could be observed by TEM or by XRD (see Figure 6).

Figure 6a shows XRD patterns of both types of $Pt/TiO_2/RuO_2$ samples. Due to the local epitaxial growth of TiO_2 on top of the RuO_2 rutile structure, pure rutile TiO_2 films were obtained with no traces of anatase phase. Decomposition of the diffraction peak located at $2\theta \approx 35°$ (Figure 6b) revealed the characteristic TiO_2 rutile peak located at 36.03° next to the RuO_2 peak located at 35.26° in both types of samples. Moreover, no characteristic peaks corresponding to Magnéli phases could be found in the XRD patterns displayed in Figure 6a, such as Ti_3O_5 (characteristic peaks located around ~25°, ~33°, and 49.2° according to PDF2 database), Ti_4O_7 (20.7° and 31.7°),[32] Ti_5O_9 (21.95°),[32] or Ti_6O_{11} (22.85°).[32]

The leakage current distribution can be influenced also by build-up of negative charge at the grain boundaries, which could arise from electron trapping or negatively charged oxygen ions. Oxygen ion mobility at grain boundaries is higher than that inside the grains,[33] which suggests not only passivation of the oxygen vacancies at the grain boundaries, but also the accumulation of excess oxygen ions at the boundaries. The electric field created by this negative charge acts toward a reduction of the leakage current. Another consequence of the accumulation of excess oxygen at the grain boundaries is a possible local increase of the electrode EWF. Oxygen's electronegativity is much higher than that of metal atoms, which means that the dipoles formed will result in an increase of EWF.

Concerning the second important observation about the fundamentally different conduction behavior of the two films (i.e., sample $TiO_2(TiCl_4)$ shows highly localized spots with rather high leakage currents in contrary to sample TiO_2(TTIP)

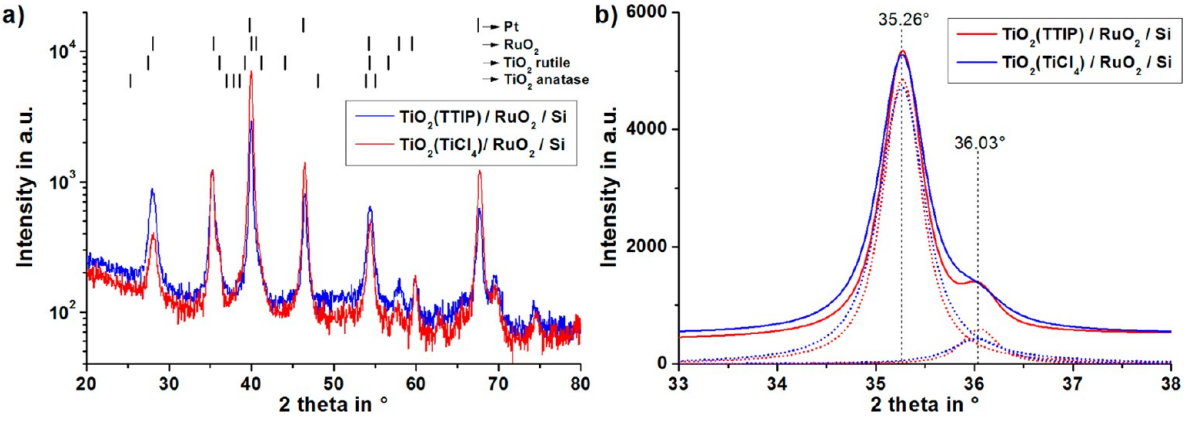

Figure 6. (a) XRD patterns of both types of $Pt/TiO_2/RuO_2$ samples with characteristic peak positions of Pt, RuO_2, and rutile and anatase TiO_2. No anatase peaks are present at 25.28° and 48.05°. (b) More detailed view at the characteristic rutile peak located at 36.03° near the RuO_2 peak at 35.26°. Dotted curves represent the decomposition of the measured curves.

with rather homogeneously distributed leakage spots of smaller leakage current) the different ALD conditions for both film types should be considered. By using TTIP precursor with its molecule incorporating 4 oxygen atoms together with the strong oxidative power of O_3 the grown TiO_2(TTIP) layers are slightly hyperstoichiometric with a Ti:O ratio of ∼1:2.1 (as measured by XPS, data not shown). The integral part of the excessive oxygen probably resides on grain boundaries, therefore, not leading to the interstitial-type defect generation which would result in p-type conduction. Moreover, as shown by first-principle and structure calculation,[34] even in TiO_2 with an overall oxygen-excessive composition, oxygen vacancies which result in n-type conduction can be formed. In any case, TiO_2($TiCl_4$) layers that are closer to stoichiometric composition[9,35] contain a higher amount of oxygen vacancies. As the localized conduction of these layers is connected with only certain very leaky grains it can be assumed that these leaky grains contain a higher amount of unevenly distributed vacancies which are arranged in a way that electrons can take advantage of these as stepping sites for the TAT current to flow. It was recently proven that the band gap state in TiO_2 originates mainly from bridging oxygen vacancies.[36] Another reason for the localized conduction might be the anisotropic nature of rutile TiO_2 where the anisotropy of crystalline grains affects anisotropy of the effective work function[37] and the effective tunneling electron mass.[38] Hence, the conductivity of the grains with specific orientation and composition will be larger. Concerning TiO_2(TTIP) layers, the oxygen vacancies are present in a very limited amount in these layers and the conduction spots are, therefore, less leaky and more homogeneously distributed.

CONCLUSIONS

In summary, nanoscale leakage current characteristics of TiO_2 layers grown on a RuO_2 electrode layer using two different ALD processes (i.e., $TiCl_4$ and H_2O at 400 °C vs TTIP and O_3 at 250 °C) were investigated by CAFM. From CAFM topography images, the crystal grain size of TiO_2 films grown using a $TiCl_4$ precursor was found to be larger than that for the films grown using a TTIP precursor, which is well consistent with plane view TEM analysis. The leakage current distribution of TiO_2 layers clearly showed a good correlation with the topography image: Higher leakage current spots were mainly located on elevated grains of the TiO_2 films and not along grain boundaries. The leakage current distribution of TiO_2 films grown using a $TiCl_4$ precursor showed larger localized spots of higher leakage current, while that grown using a TTIP precursor showed smaller homogeneously distributed leakage spots of relatively low leakage current. Besides, the overall leakage current level of the $TiCl_4$ based layers was found to be larger than that of the TTIP based layers. These results were well consistent with macroscopic leakage current density−voltage characteristics. These findings are important for a further reduction of the leakage current of rutile type TiO_2 films.

ASSOCIATED CONTENT

Supporting Information

Superimposed leakage current density and topography maps are presented to better visualize the correlation between topography and leakage current density for both samples. In addition, detailed series of voltage dependence of topography and current distribution maps are given for both samples to proof the reproducibility and reliability of the CAFM measurements. Finally, X-ray reflectivity (XRR) measurements are provided from which the TiO_2 thickness was precisely evaluated. This material is available free of charge via the Internet at http://pubs.acs.org.

AUTHOR INFORMATION

Corresponding Author

*E-mail: mathias.rommel@iisb.fraunhofer.de.

Present Addresses

▽K.M.: Institute of Applied Physics, University of Tsukuba, 1-1-1 Tennodai, Tsukuba, Ibaraki 305-8573, Japan.

○J.H.H.: Advanced Materials Division, Korea Research Institute of Chemical Technology, 141 Gajeong-Ro, Yuseong-Gu, Daejeon 305-600, Korea.

Notes

The authors declare no competing financial interest.

ACKNOWLEDGMENTS

This work was supported by the German Federal Ministry of Education and Research (BMBF) (Project 01M3089E), Slovak grant agency Projects VEGA 2/0147/11 and APVV-0509-10, Estonian Ministry of Education and Research (Project IUT2-24) and Estonian Centre of Excellence in Research (Project TK117). C.S.H. acknowledges the support of the Converging Research Center Program through the National Research Foundation of Korea (NRF), funded by the Ministry of Education, Science, and Technology (2012K001299) of the Korean government.

REFERENCES

(1) Fröhlich, K.; Ťapajna, M.; Rosová, A.; Dobročka, E.; Hušeková, K.; Aarik, J.; Aidla, A. *Electrochem. Solid-State Lett.* **2008**, *11*, G19−G21.

(2) Han, J. H.; Han, S.; Lee, W.; Lee, S. W.; Kim, S. K.; Gatineau, J.; Dussarrat, C.; Hwang, C. S. *Appl. Phys. Lett.* **2011**, *99*, 022901-1−022901-3.

(3) Semiconductor Industry Association. *International Technology Roadmap for Semiconductors*, 2011 Edition, http://www.itrs.net.

(4) Kim, S. K.; Lee, S. W.; Han, J. H.; Lee, B.; Han, S.; Hwang, C. S. *Adv. Funct. Mater.* **2010**, *20*, 2989−3003.

(5) Lee, S. W.; Han, J. H.; Kim, S. K.; Han, S.; Lee, W.; Hwang, C. S. *Chem. Mater.* **2011**, *23*, 976−983.

(6) Knauth, P.; Tuller, H. L. *J. Appl. Phys.* **1999**, *85*, 897−902.

(7) Kim, S. K.; Kim, W.-D.; Kim, K.-M.; Hwang, C. S. *Appl. Phys. Lett.* **2004**, *85*, 4112−4114.

(8) Fröhlich, K.; Aarik, J.; Ťapajna, M.; Rosová, A.; Aidla, A.; Dobročka, E.; Hušeková, K. *J. Vac. Sci. Technol., B: Microelectron. Nanometer Struct.—Process., Meas., Phenom.* **2009**, *27*, 266−270.

(9) Fröhlich, K.; Hudec, B.; Aarik, J.; Tarre, A.; Machajdík, D.; Kasikov, A.; Hušeková, K.; Gaži, Š. *Microelectron. Eng.* **2011**, *88*, 1525−1528.

(10) Hudec, B.; Hušeková, K.; Tarre, A.; Han, J. H.; Han, S.; Rosová, A.; Lee, W.; Kasikov, A.; Song, S. J.; Aarik, J.; Hwang, C. S.; Fröhlich, K. *Microelectron. Eng.* **2011**, *88*, 1514−1516.

(11) Aarik, J.; Hudec, B.; Hušekova, K.; Rammula, R.; Kasikov, A.; Arroval, T.; Uustare, T.; K. Fröhlich, K. *Semicond. Sci. Technol.* **2012**, *27*, 074007−1 - 074007−6.

(12) De Wolf, P.; Brazel, E.; Erickson, A. *Mater. Sci. Semicond. Process.* **2001**, *4*, 71−76.

(13) Yanev, V.; Rommel, M.; Lemberger, M.; Petersen, S.; Amon, B.; Erlbacher, T.; Bauer, A. J.; Ryssel, H.; Paskaleva, A.; Weinreich, W.; Fachmann, C.; Heitmann, J.; Schroeder, U. *Appl. Phys. Lett.* **2008**, *92*, 252910-1−252910-3.

(14) Murakami, K.; Rommel, M.; Yanev, V.; Bauer, A. J.; Frey, L. *AIP Conf. Proc.* **2011**, *1395*, 134−138.
(15) Yanev, V.; Erlbacher, T.; Rommel, M.; Bauer, A. J.; Frey, L. *Microelectron. Eng.* **2009**, *86*, 1911−1914.
(16) Iglesias, V.; Martin-Martinez, J.; Porti, M.; Rodriguez, R.; Nafria, M.; Aymerich, X.; Erlbacher, T.; Rommel, M.; Murakami, K.; Bauer, A. J.; Frey, L.; Bersuker, G. *Microelectron. Eng.* **2013**, *109*, 129−132.
(17) Hofer, A.; Biberger, R.; Benstetter, G.; Wilke, B.; Göbel, H. *Microelectron. Reliab.* **2013**, *53*, 1430−1433.
(18) Foissac, R.; Blonkowski, S.; Kogelschatz, M.; Delcroix, P.; Gros-Jean, M.; Bassani, F. *Microelectron. Reliab.* **2013**, *53*, 1857−1862.
(19) Rommel, M.; Jambreck, J. D.; Lemberger, M.; Bauer, A. J.; Frey, L.; Murakami, K.; Richter, C.; Weinzierl, P. *J. Vac. Sci. Technol., B: Microelectron. Nanometer Struct.—Process., Meas., Phenom.* **2013**, *31*, 01A108-1−7.
(20) Polspoel, W.; Vandervorst, W.; Aguilera, L.; Porti, M.; Nafria, M.; Aymerich, X. *Mater. Res. Soc. Symp. Proc.* **2008**, *1074*, 94−100.
(21) Menou, N.; Popovici, M.; Clima, S.; Opsomer, K.; Polspoel, W.; Kaczer, B.; Rampelberg, G.; Tomida, K.; Pawlak, M. A.; Detavernier, C.; Pierreux, D.; Swerts, J.; Maes, J. W.; Manger, D.; Badylevich, M.; Afanasiev, V.; Conard, T.; Favia, P.; Bender, H.; Brijs, B.; Vandervorst, W.; Van Elshocht, S.; Pourtois, G.; Wouters, D. J.; Biesemans, S.; Kittl, J. A. *J. Appl. Phys.* **2009**, *106*, 094101-1−094101-7.
(22) Iglesias, V.; Porti, M.; Nafría, M.; Aymerich, X.; Dudek, P.; Schroeder, T.; Bersuker, G. *Appl. Phys. Lett.* **2010**, *97*, 262906−1−262906−3.
(23) Menou, N.; Wang, X. P.; Kaczer, B.; Polspoel, W.; Popovici, M.; Opsomer, K.; Pawlak, M. A.; Knaepen, W.; Detavernier, C.; Blomberg, T.; Pierreux, D.; Swerts, J.; Maes, J. W.; Favia, P.; Bender, H.; Brijs, B.; Vandervorst, W.; Van Elshocht, S.; Wouters, D. J.; Biesemans, S.; Kittl, J. A. In *Electron Devices Meeting*, Proceedings of the IEEE International Conference, San Francisco, CA, Dec 15−17, 2008; Deleonibus, S., Ed.; Institute of Electrical and Electronics Engineers, Inc.: Piscataway, NJ, 2008.
(24) Ikeda, H.; Goto, T.; Sakashita, M.; Sakai, A.; Zaima, S.; Yasuda, Y. *Jpn. J. Appl. Phys.* **2003**, *42*, 1949−1953.
(25) Lanza, M.; Iglesias, V.; Porti, M.; Nafria, M.; Aymerich, X. *Nanoscale Res. Lett.* **2011**, *6*, 108-1−108-9.
(26) Lanza, M.; Porti, M.; Nafría, M.; Aymerich, X.; Whittaker, E.; Hamilton, B. *Rev. Sci. Instrum.* **2010**, *81*, 106110-1−106110-3.
(27) Shin, J. C.; Park, J. H.; Hwang, C. S.; Kim, H. J. *J. Appl. Phys.* **1999**, *86*, 506−513.
(28) Seo, M.; Rha, S. H.; Kim, S. K.; Han, J. H.; Lee, W.; Han, S.; Hwang, C. S. *J. Appl. Phys.* **2011**, *110*, 024105-1−024105-7.
(29) Liborio, L.; Harrison, N. *Phys. Rev. B: Condens. Matter Mater. Phys.* **2008**, *77*, 104104-1−104104-10.
(30) Tu, R.; Hou, G.; Kimura, T.; Goto, T. *Thin Solid Films* **2010**, *518*, 6927−6932.
(31) Kwon, D. H.; Kim, K. M.; Jang, J. H.; Jeon, J. M.; Lee, M. H.; Kim, G. H.; Li, X. S.; Park, G. S.; Lee, B.; Han, S.; Kim, M.; Hwang, C. S. *Nat. Nanotechnol.* **2010**, *5*, 148−153.
(32) Regonini, D.; Dent, A. C. E.; Bowen, C. R.; Pennock, S. R.; Taylor, J. *Mater. Lett.* **2011**, *65*, 3590−3592.
(33) Rothschild, A.; Komem, Y.; Cosandey, F. *Interface Sci.* **2001**, *9*, 157−162.
(34) Kamisaka, H.; Yamashita, K. *J. Phys. Chem. C* **2011**, *115*, 8265−8273.
(35) Aarik, J.; Aidla, A.; Mändar, H.; Uustare, T. *Appl. Surf. Sci.* **2001**, *172*, 148−158.
(36) Yim, C. M.; Pang, C. L.; Thornton, G. *Phys. Rev. Lett.* **2010**, *104*, 036806-1−036806-4.
(37) Hölzl, J.; Schulte, F. K.; Wagner, H. *Springer Tracts Mod. Phys.* **1979**, *85*, 1−50.
(38) Perevalov, T. V.; Gritsenko, V. A. *J. Exp. Theor. Phys.* **2011**, *112*, 310−316.